PHYSICAL REVIEW E **73**, 046701 (2006)

Multidimensional reactive scattering with quantum trajectories

Robert E. Wyatt* and Dmytro Babyuk
Department of Chemistry and Biochemistry, Institute for Theoretical Chemistry, The University of Texas, Austin, Texas 78712, USA

(Received 2 December 2005; published 10 April 2006)

Ensembles of quantum trajectories are evolved to study time-dependent reaction dynamics in multidimensional systems with up to 25 vibrational modes. The equations of motion are formulated in curvilinear reaction path coordinates and all coupling terms are retained, including those involving curvature of the reaction path. The model potential is a Gaussian barrier along the translational coordinate coupled to M vibrational modes. Spatial derivatives needed to propagate the trajectories are evaluated by least squares fitting in a contracted basis set. Stable propagation of the trajectory ensembles was carried out until complete bifurcation into reflected and reactive subensembles. The reaction probabilities were evaluated by Monte Carlo integration of the multidimensional smooth transmitted densities. Computational results, including trajectory plots and time-dependent reaction probabilities, are presented for $M=1$, 5, and 25 vibrational modes.

DOI: 10.1103/PhysRevE.73.046701 PACS number(s): 02.70.Ns, 03.65.Nk, 34.50.−s

I. INTRODUCTION

Ensembles of quantum trajectories have recently been used to study the quantum dynamics of multidimensional systems, although, in a number of cases, two degrees of freedom were involved. As background for the current studies, the earlier multidimensional work will be briefly reviewed. In the first application of quantum trajectories to reactive scattering, Wyatt studied the trajectory dynamics for a model collinear reaction [1]. In this formulation, reaction path curvature was included in the equations of motion for the trajectories and spatial derivatives were evaluated by a least squares method. Using a Delaunay tessellation method for function fitting and derivative evaluation, Nerukh and Frederick [2] propagated quantum trajectories in two and three dimensions. Instructive plots showed bifurcation of the probability density during the scattering process. In addition, Rabitz and co-workers [3,4] used ensembles of quantum trajectories to propagate wave packets for two-dimensional models representing the photodissociation of NOCl and NO_2. Quantum trajectories were used by Wyatt to study electronic nonadiabatic effects for two coupled 11 degrees of freedom potential energy surfaces [5], and Na and Wyatt studied the decay of a metastable state in models with up to 15 degrees of freedom [6]. Recently, Kendrick reported time-dependent reaction probabilities for an M-dimensional reactive scattering model [7] which included reaction path curvature. This approach used an arbitrary Lagrangian-Eulerian (ALE) moving frame along with a regridding algorithm to create or annihilate trajectories as needed in order to maintain uniform spacing. In order to counter the growth of computational effort with increasing values of M, a decoupling approximation was introduced in order to decompose the problem into a set of one-dimensional problems. Computational results were reported for values of M through 100.

In addition, Pauler and Kendrick [8] propagated ensembles of quantum trajectories for a two-dimensional reactive scattering model (with neglect of reaction path curvature). In order to circumvent problems arising from node formation, artificial viscosity terms were added to the equations of motion. In a study of scattering from a barrier in a two-dimensional model [9], Babyuk and Wyatt applied the covering function method [10] to deal with the node problem. With this method, it was possible to evolve trajectory ensembles for long times, even for wave packets which were vibrationally excited in the initial state. Starting from an initial nonstationary state represented by quantum trajectories, Maddox and Bittner [11] propagated quantum trajectories in order to compute the ground state for the bend-stretch vibrational modes of CH_3I.

By modeling the nonclassical component of the momentum operator, Garashchuk and Rassolov developed an approximate quantum potential [12–14] (AQP). This method was used to compute energy-resolved reaction probabilities for the collinear $H+H_2$ reaction and photodissociation spectra for a two-dimensional model of ICN. Using an AQP, Rassolov *et al.* computed reaction probabilities for the $O(^3P)+H_2$ (and HD) reactions in three-dimensional space in the absence of rotational motion [15]. Excellent quantum trajectory results were obtained in comparison with those computed using conventional propagation techniques.

The main obstacle to straightforward propagation of quantum trajectory ensembles is the node problem [16]. In regions where nodes form in the wave function, the quantum potential may become singular and this makes accurate trajectory propagation difficult. Fortunately, several methods have been developed to resolve this issue [16]. In scattering problems involving barrier transmission, node formation usually occurs in the incident channel during the time interval that the wave packet is undergoing bifurcation. In the current study, we will not apply any of the methods for handling the node problem because the focus is upon transmission of probability density to the product channel. Even though we will not obtain accurate reflected wave packets, the transmitted packet, which is smooth, can be accurately computed. In addition, if the barrier is relatively low, then nodes forming in the reflected packet do not significantly disturb the transmitted portion of the packet.

---

*Corresponding author. Email address: wyattre@mail.utexas.edu

The purpose of the present study is to develop and apply an algorithm for propagation of ensembles of quantum trajectories undergoing reactive scattering in multidimensional systems. (However, since rotational and angular momentum effects have not been incorporated, the present formulation may be most appropriate for condensed phase reactive processes.) The equations of motion are developed in curvilinear reaction path coordinates (RPC) and all coupling terms are retained in the equations of motion, including those involving reaction path curvature. For the case where only one vibrational mode is coupled to motion along the reaction coordinate, the trajectory results will be compared with those obtained by directly integrating the time-dependent Schrödinger equation on a large spatial grid. In addition, computational results will be presented for scattering problems in which the number of vibrational modes is much larger (up to 25).

Because reaction path coordinates blend smoothly from the reactant region through the collision complex into the product region, they have been used in a number of statistical and dynamical studies of reaction dynamics. Arguably, these coordinates provide the best framework for performing dynamical analysis, such as studies of energy transfer, in the collision complex. However, a major disadvantage of this approach arises from the complexity of the kinetic energy operator. For this reason, it is also important to explore the propagation of trajectory ensembles in other coordinate systems, such as Cartesian and Jacobi. In this regard, it is significant that the quantum trajectory studies mentioned earlier for the $O(^3P)+H_2$ reaction [15] were performed in Jacobi coordinates.

The organization of the remainder of this paper is as follows: In Sec. II, the reaction path Hamiltonian is constructed and Lagrangian trajectory equations of motion are derived. The model potential energy surface, generation of initial conditions for the trajectories, implementation of a least squares routine for spatial derivative evaluation and function interpolation, and Monte Carlo integration of the multidimensional probability density are also described in Sec. II. In Sec. III, results are presented for wave packet evolution in systems for which the number of vibrational modes varies from 1 through 25. Finally, a brief summary is presented in Sec. IV.

II. REACTIVE SCATTERING WITH QUANTUM TRAJECTORIES

A. Reaction path coordinates and kinetic energy

The Hamiltonian and equations of motion for the hydrodynamic fields will be formulated in orthogonal curvilinear RPC. The approach used here differs in some aspects from the natural collision coordinate formulation of Marcus [17] and from the later reaction path Hamiltonian (RPH) developed by Miller, Handy, and Adams [18]. Starting in Jacobi coordinates for the reactants, we construct a reference curve (RC) which leads from the reactant region through the collision complex and into the product region. In this study, it will be assumed that the RC is planar. The arc length measured along this curve (s) is negative in reactants and positive in products. The origin for s is arbitrary, but in this study will be chosen at the position of the barrier maximum in the collision complex. The RC follows the minimum potential energy in the asymptotic reactant and product channels, but does not necessarily pass through the saddle point (if there is one) in the collision complex. In general, the RC and the steepest descent path leading away from the saddle point may be displaced from each other by the vector $\vec{d}(s)$. However, in this study, this displacement will be assumed to vanish.

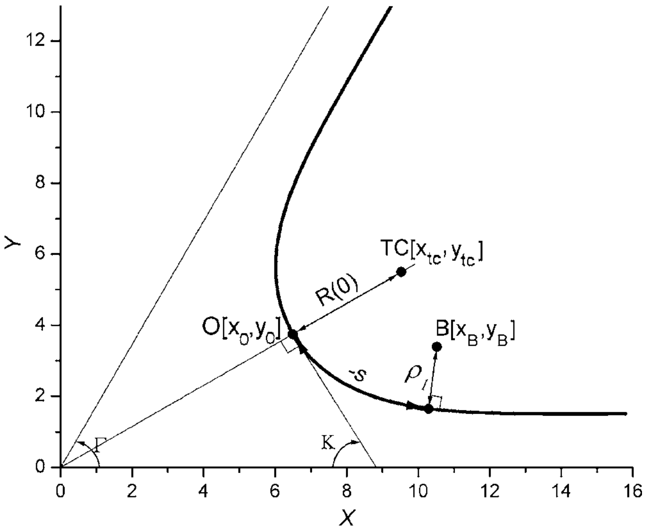

FIG. 1. RC plotted in Cartesian coordinates (measured in a.u.). Parameter values are given in Table I. The geometric quantities are defined in Sec. II A.

The RC is characterized by the curvature $\kappa(s)$, which vanishes at large distances from the collision complex. We will assume that the curvature has a Gaussian form

$$\kappa(s) = A\exp(-\alpha s^2) = \frac{d\varphi}{ds}, \tag{2.1}$$

where $\varphi(s)$ is the angle (measured clockwise) between tangents to the RC at points s and the asymptotic reactant region [in this study, $\varphi(0)=\pi/3$]. The reciprocal of the curvature defines the turning radius, $R(s)=1/\kappa(s)$, and this quantity is used to specify one of the constants in the equation for the curvature: $A=1/R(0)$. In order to specify the RC in Cartesian coordinates, the turning center (x_{tc},y_{tc}) and the skew angle Γ are needed in addition to $R(0)$ (see Fig. 1). It is then straightforward to derive the Cartesian coordinates of the saddle point (x_0,y_0) (see Table I). Starting from this point and taking into account that

$$dx = -ds\cos[\varphi(s)], \tag{2.2}$$

$$dy = ds\sin[\varphi(s)], \tag{2.3}$$

the RC is constructed by integration of Eqs. (2.1)–(2.3),

$$\varphi(s) = \frac{1}{2R(0)}\sqrt{\frac{\pi}{\alpha}}\,\mathrm{erf}(\sqrt{\alpha}s) + K, \tag{2.4}$$

TABLE I. Parameters for the reference curve in Fig. 1 (all units are atomic).

$R(0)=3.5, \quad \Gamma=\frac{\pi}{3}$	$s_B=-4.5,\ \rho_{1B}=1.75$
$K=\frac{1}{2}(\pi-\Gamma)=\frac{\pi}{3}$	$x^s(s_B)=x_0-\int_0^{s_B}\cos\phi(s')ds'=10.29$
$\alpha=\frac{\pi}{R(0)^2(\pi-\Gamma)^2}=0.058$	$y^s(s_B)=y_0+\int_0^{s_B}\sin\phi(s')ds'=1.65$
$y_{tc}=5.50, \quad x_c=\frac{y_{tc}}{\tan(\Gamma/2)}=9.53$	$x(s_B,\rho_{1B})=x^s(s_B)+\rho_{1B}\sin[\phi(s_B)]=10.52$
$x_0=x_{tc}-R(0)\cos(\Gamma/2)=6.50$ $y_0=y_{tc}-R(0)\sin(\Gamma/2)=3.75$	$y(s_B,\rho_{1B})=y^s(s_B)+\rho_{1B}\cos[\phi(s_B)]=3.59$

$$x^s(s)=x_0-\int_0^s\cos\varphi(s')ds', \tag{2.5}$$

$$y^s(s)=y_0+\int_0^s\sin\varphi(s')ds'. \tag{2.6}$$

The integrals in Eqs. (2.5) and (2.6) are computed numerically. The angle K between the RC tangents at the position $s=0$ and the asymptotic reactant region ($s\rightarrow-\infty$) is related to Γ by $K=\frac{1}{2}(\pi-\Gamma)$. From another viewpoint, angle K can also be found from Eq. (2.4)

$$K=\varphi(0)-\varphi(-\infty)=\frac{1}{2R(0)}\sqrt{\frac{\pi}{\alpha}}. \tag{2.7}$$

As a result, parameter α in Eq. (2.1) is determined by $R(0)$ and Γ,

$$\alpha=\frac{\pi}{R(0)^2(\pi-\Gamma)^2}. \tag{2.8}$$

This relationship guarantees that the RC is a straight line in the asymptotic regions.

Turning to the vibrational degrees of freedom, the vibrational coordinate in the plane specified by the RC is denoted ρ_1 (this is the perpendicular distance from a point to the RC and it is chosen to be positive on the concave side of the RC). The relations between the curvilinear and Cartesian coordinates for any arbitrary point are

$$x(s,\rho_1)=x^s(s)+\rho_1\sin[\varphi(s)], \tag{2.9}$$

$$y(s,\rho_1)=y^s(s)+\rho_1\cos[\varphi(s)]. \tag{2.10}$$

The RC for the particular set of parameters and correspondence between the curvilinear (s,ρ_1) and Cartesian (x,y) coordinates for an arbitrary point B is demonstrated in Fig. 1 and Table I.

In the kinetic energy operator, the two "planar coordinates" (s,ρ_1) are coupled by curvature terms. For a system with M vibrational modes, at each value for s, the remaining $(M-1)$ vibrational coordinates span a hyper-space orthogonal to the RC. The M vibrational displacements from the RC are denoted by ρ_i $(i=1,2,\ldots M)$. As we progress along the RC, the vibrational hyper-space "swings around" the RC, always remaining orthogonal to it.

In terms of RPC, the kinetic energy operator $\hat{K}$ is given by

$$-\frac{\hbar^2}{2\mu}\nabla^2=-\frac{\hbar^2}{2\mu}\left[\eta^{-1}\partial_s(\eta^{-1}\partial_s)+\eta^{-1}\partial_{\rho_1}(\eta\partial_{\rho_1})+\sum_{j=2}^{M}\partial_{\rho_j\rho_j}\right], \tag{2.11}$$

in which we use the notation $\partial_s=\partial/\partial s$, μ is the reduced mass, and where $\eta=1-\kappa(s)\rho_1$. In this equation, the two planar coordinates (s,ρ_1) are coupled by the curvature term η, but the remaining $(M-1)$ vibrational coordinates ρ_j $(2\leqslant j\leqslant M)$ are not coupled by curvature terms to the two planar coordinates. (If the RC becomes nonplanar, there are additional curvature/torsional coupling terms between s and the vibrational coordinates.)

The kinetic energy operator in Eq. (2.11) does not have the form used in the RPH derived by Miller *et al.* [18]. In that study, local normal vibrational coordinates were introduced and these twist around the RC during the progression from reactants to products. As a result, complicated dynamical coupling terms appear in their kinetic energy operator. In our case, an invariant orientation is used for the vibrational coordinates throughout the reaction space and vibration-vibration coupling is thus transferred to the potential energy term in the Hamiltonian (i.e., local normal modes are not introduced).

B. Model potential energy surface

The model potential energy surface used for this study is constructed from a Gaussian barrier in the translational coordinate coupled to a harmonic bath with M vibrational modes

$$U(s,\rho_1,\rho_2,\ldots\rho_M) = V_0\exp(-as^2) + \frac{1}{2}\sum_{i=1}^{M} k_i(s)\rho_i^2. \tag{2.12}$$

Coupling between the translational and vibrational coordinates is introduced via the s-dependent force constants $k(s)$, defined by

$$k_i(s) = k_{0i}[1-\bar{\sigma}\exp(-bs^2)]. \tag{2.13}$$

The coupling parameter $\bar{\sigma}$ in this equation must be rescaled due to the complexity of the potential for high dimensionality. For example, if $a=b$, then upon substituting Eq. (2.13) into Eq. (2.12), the potential energy can be rewritten as

$$U(s,\rho_1,\rho_2,\ldots\rho_M) = \exp(-as^2)\left[V_0 - \frac{\bar{\sigma}}{2}\sum_{i=1}^{M} k_{i0}\rho_i^2\right] + \frac{1}{2}\sum_{i=1}^{M} k_{i0}\rho_i^2. \tag{2.14}$$

When $\rho_i \neq 0$, the second term within the square brackets is subtracted from V_0, thus lowering the effective barrier. This effect becomes more significant as the number of vibrational modes grows due to the summation in the second term within the brackets. Moreover, it can even happen that the second term in the brackets exceeds V_0. As a result, a basin forms instead of a barrier along the translational coordinate at fixed ρ_i. In this case, the dynamics will be very complex. In order to avoid formation of the potential well in regions accessible to parts of the wave packet, the coupling parameter $\bar{\sigma}$ should be chosen appropriately. One way is to divide it by M, thus compensating growth of the sum within the brackets in Eq. (2.14) as the dimensionality increases. Based upon this consideration, our final model potential energy is defined as

$$U(s,\rho_1,\rho_2,\ldots\rho_M) = V_0\exp(-as^2) + \frac{1}{2}\sum_{i=1}^{M} k_{i0}[1-(\sigma/M)\exp(-bs^2)]\rho_i^2. \tag{2.15}$$

The parameters used in this study are as follows: $a=1.5$ a.u., $\sigma=0.1$ a.u., $b=1.5$ a.u., $V_0=1000$, 2000, and 3000 cm^{-1}. The force constants k_{0i} are uniform random numbers in the interval $k_{\min}<k_{0i}<k_{\max}$, where $k_{\min}=0.7k_{\max}$, and $k_{\max}$ is chosen to make a one-dimensional harmonic potential equal to 10 000 cm^{-1} when $\rho_i=1$ a.u.

C. Lagrangian equations of motion

Now that the kinetic and potential energy operators have been expressed in reaction path coordinates, equations of motion for the hydrodynamic fields can be derived. This derivation is initiated by substituting the polar form for the wave function, $\psi=\exp(C+iS/\hbar)$, into the time-dependent Schrödinger equation. In the polar form, the amplitude C and the action function S are both real valued. After some simplification, we obtain equations of motion for the two fields

$$\frac{dC}{dt} = -\frac{1}{2\mu}\left[\frac{S_{ss}}{\eta^2} - \frac{\kappa}{\eta}S_{\rho_1} + \frac{\kappa_s}{\eta^3}\rho_1 S_s + \sum_{j=1}^{M} S_{\rho_j\rho_j}\right], \tag{2.16}$$

$$\frac{dS}{dt} = \frac{1}{2\mu}\left[\frac{S_s^2}{\eta^2} + \sum_{j=1}^{M} S_{\rho_j}^2\right] - (U+Q), \tag{2.17}$$

where subscript notation has been used for partial derivatives, $C_s=\partial C/\partial s$, $C_{ss}=\partial^2 C/\partial s^2$, etc. The curvature or its derivative explicitly enters several terms in these two equations. The right side of Eq. (2.17) constitutes the quantum Lagrangian, the excess of the local kinetic energy over the total potential energy (the sum of U and Q). In terms of RPCs, the quantum potential in Eq. (2.17) is given by

$$Q = -\frac{\hbar^2}{2\mu}\left[\frac{1}{\eta^2}(C_{ss}+C_s^2) + \frac{\kappa_s}{\eta^3}\rho_1 C_s + \sum_{j=1}^{M}(C_{\rho_j\rho_j}+C_{\rho_j}^2) - \frac{\kappa}{\eta}C_{\rho_1}\right]. \tag{2.18}$$

We note that the reaction path curvature enters into several terms in the quantum potential.

Equations (2.16) and (2.17) have been expressed in the Lagrangian frame, in which each grid point moves at the local flow velocity of the probability fluid, and the resulting dynamics is then expressed in terms of Bohmian trajectories. Quantum dynamics in more general arbitrary Lagrangian-Eulerian frames is described elsewhere [16].

D. Initial conditions

The initial wave function is assumed to be the product of a normalized Gaussian wave packet for the translational motion multiplied by a plane wave and M one-dimensional ground state harmonic oscillator functions for the vibrational motion

$$\Psi(s,\rho_1,\rho_2\ldots\rho_M) = \sqrt[4]{\frac{2\beta_s}{\pi}}\exp(iks)\exp[-\beta_s(s-s_0)^2] \times\prod_{i=1}^{M}\sqrt[4]{\frac{2\beta_{\rho i}}{\pi}}\exp(-\beta_{\rho i}\rho_i^2). \tag{2.19}$$

The probability density is then discretized into an ensemble of N particles. These grid points form an irregular structure in $(M+1)$-dimensional space, with the points scattered around the point of maximum probability density. It is desirable that each particle carry a probability density which lies above a minimum threshold value.

In order to define the initial coordinates for these quantum trajectories, each particle's coordinate was randomly generated according to the normal distribution with mean values $\langle s\rangle = s_0$, $\langle \rho_i\rangle = 0$, and optimized standard deviations. If the standard deviations are too low, then the particles cluster around the maximum point and sample only part of the probability density. At the other extreme, values of the standard deviations which are too large make the particles spread into regions of very low probability density where they are useless. The optimal standard deviations are inversely related to square roots of the width parameters (β) in Eq. (2.19). Even at optimized standard deviations, a few generated particles fall into regions of low probability density and they are dropped from the ensemble.

E. Determination of derivatives through least squares fitting

From information carried at the scattered trajectory locations (namely, the functions C and S), it is necessary to compute spatial derivatives of the hydrodynamic fields in order to integrate Eqs. (2.16) and (2.17). Least squares fitting provides a method for doing this [16]. Within a stencil of n_p nearest points encompassing the point of interest, the function is expanded in a local basis set $\{p_j(\vec{r})\}$ comprising n_b terms, with $n_p > n_b$. At each point in the stencil, we would like approximant $f(\vec{r})$ to satisfy the equations

$$f(\vec{r}_i) = \sum_{j=1}^{n_b} p_j(\vec{r}_i) a_j, \quad i = 1, 2, \ldots n_p, \tag{2.20}$$

in which the coefficients $\{a_j\}$ are to be determined. Since there are typically many more of these equations than unknowns, the system is said to be overdetermined. Once the fitting coefficients have been computed, the spatial derivatives are determined from the derivatives of the basis functions. For example, the first derivative with respect to coordinate q_k is given by

$$\frac{\partial f}{\partial q_k} = \sum_{j=1}^{n_b} \frac{\partial p_j}{\partial q_k} a_j. \tag{2.21}$$

In matrix notation, Eq. (2.20) becomes

$$Pa = f, \tag{2.22}$$

where the rectangular matrix P (dimension $n_p \times n_b$) has elements $P_{i,j} = p_j(\vec{r}_i)$. The other two matrices are column vectors with n_b or n_p rows for a or f, respectively.

The usual way to solve these equations is to weight each equation, form the normal equations, $P^t w P a = P^t w f$, and then find the inverse of the $P^t w P$ matrix

$$a = (P^t w P)^{-1}(P^t w f), \tag{2.23}$$

where P^t denotes the transpose [19,20]. The diagonal weight matrix is frequently chosen to have Gaussian elements

$$w_{i,i} = \exp(-\omega r_i^2). \tag{2.24}$$

The inverse matrix in Eq. (2.23) can be computed by LU decomposition followed by back substitution. In addition, since the $P^t w P$ matrix is symmetric and positive definite, it can be factored by Cholesky decomposition, thus spending less computational time than LU decomposition [21]. Although this approach sometimes works very well, the method breaks down when the columns or rows of $P^t w P$ approach linear dependence. When there is near linear dependence, the condition number of $P^t w P$ becomes very large and the resulting solution vector a may not be accurate.

Instead of proceeding through the normal equations, we will "directly" solve the weighted matrix equation (2.22) for the solution vector

$$a = (wP)^{+} w f, \tag{2.25}$$

where $(wP)^{+}$ is the Moore-Penrose generalized inverse of the rectangular matrix. There are several ways to determine $(wP)^{+}$ [19,20]. The first involves orthogonalization of the columns of wP via the QR transform: $wP = QR$ (the orthogonal matrix Q has dimensions $n_p \times n_b$ and the upper triangular matrix R has dimensions $n_b \times n_b$). In terms of these two matrices, the pseudoinverse is given by $(wP)^{+} = R^{-1} Q^t$. A second method for determination of the pseudoinverse involves the singular value decomposition (SVD) of the matrix wP: $wP = UDV^t$ (the dimensions of U, D, and V are $n_p \times n_b$, $n_b \times n_b$, and $n_b \times n_b$, respectively). In this factorization, the diagonal matrix D stores the "singular values" while U and V are orthogonal matrices. In terms of these matrices, the pseudoinverse is given by $(wP)^{+} = VD^{-1}U^t$.

Formation of the pseudoinverse through either of these factorizations provides an effective means of solving the least squares equations. We have used both of these methods in the applications of quantum trajectory methods to reaction dynamics. Specific values for n_p and n_b will be mentioned in Sec. III.

In order to form the stencil for a particular particle, distances between this particle and all others must be found and then sorted by increasing value. This process may be time consuming since $(N-1)$-dimensional vectors for N particles must be sorted. However, there is no need to do this at every time step. Quantum trajectories do not suddenly change their relative positions in the ensemble during evolution. Therefore, resorting is only performed periodically (every 50–100 atomic time units). This procedure significantly reduces the computational time.

Concerning the choice of basis set in Eq. (2.20), it is desirable to include as many functions as possible. However, it is also important to restrict n_b to keep the computer time as small as possible. For this reason, we limit the complexity of the basis sets by eliminating some terms that would occur in the direct product of terms from the separate coordinates. Consider $M=2$, for example, and let $\{x, y_1, y_2\}$ denote translational and vibrational displacements from the reference point. The basis set that we use, denoted B, is complete through linear and diagonal quadratic terms, but restricted in the number of off-diagonal quadratic and cubic terms

$$B = \{1, x, y_1, y_2, x^2, y_1^2, y_2^2, xy_1, x^3, x^2 y_1, xy_1^2\}. \tag{2.26}$$

In this basis, higher-order terms in x and y_1 are included because these modes are expected to be strongly coupled by curvature terms in the Hamiltonian. For the general case with

M vibrational modes, the dimension of this basis set is given by $d=2M+7$ and the size only grows linearly with M. Even for 100 modes, the dimension of the basis is manageable, $d=207$. For low values of $M(\leqslant 25)$, inclusion of additional quadratic and cubic terms in the basis set was found to produce only minor changes in the trajectory dynamics.

F. Monte Carlo computation of reaction probabilities

One goal of these quantum trajectory calculations involves the computation of reaction probabilities. Integration of the probability density needs to be carried out over the region of this space where the scattered data is distributed. Since the initial trajectories were generated at random according to the normal distribution, each trajectory carries the same weight, $w=1/N$. Then the reaction probability is simply the ratio of the number of transmitted trajectories to the total number of trajectories [15]. However, the total number of trajectories should be relatively large (at least several thousand) in order to give accurate reaction probabilities.

In this study, an alternate Monte Carlo technique was developed for computing the transmission probabilities, even when the number of trajectories is small. The integration region is sampled by random Monte Carlo points and the probability density at each of these points is computed from information carried by the scattered trajectories. (Trajectories exterior to the integration region are ignored.) If the Monte Carlo points are sampled using a normalized probability density p, then according to the basic Monte Carlo theorem, the integral of any function f is estimated by [22]

$$\int f dV \approx \left\langle \frac{f}{p} \right\rangle \pm \mathrm{Err}, \tag{2.27}$$

where Err is the standard deviation error estimate for the integral and is given by

$$\mathrm{Err} = \sqrt{\frac{\langle f^2/p^2\rangle - \langle f/p\rangle^2}{N_{mc}}}, \tag{2.28}$$

where N_{mc} is the number of sample points. The efficiency of Eq. (2.27) depends mainly on the choice of the sampling density p. In our case, the best choice for p is the multivariate normal distribution. The region of scattered data should be sampled in such a way that only a small portion of the sample points fall beyond the region encompassed by the data. This match can be achieved by varying the mean and standard deviation values for the normal density p. During computation of the reaction probability, only sample points with $s > s_b$ are included, where s_b is the left boundary of the transmitted subensemble.

The probability density at a sample point is computed via interpolation from the scattered data. The method used here is the same least squares fitting procedure that was used for derivative evaluation. This method is easily adapted for function evaluation at any arbitrary point. Similar to the method described earlier, one creates a stencil for the Monte Carlo sample point with n_p nearest quantum trajectories and then finds the least squares coefficients. Of course, this approach is relatively time consuming since the stencil must be formed for each Monte Carlo sample point. Accuracy of the Monte Carlo integration is controlled by the value of Err in Eq. (2.28). When $N_{mc}=10^4$ and optimal mean and standard deviation values are used for p [see Eq. (2.27)], the error falls in the range Err=0.007–0.010. If higher accuracy is needed, N_{mc} should be raised. For the computations reported in Sec. III for some unfavorable cases, the highest number of Monte Carlo points was $N_{mc}=10^5$.

III. COMPUTATIONAL RESULTS

We will first consider the reactive scattering problem where only one vibrational mode is coupled to translational motion along the RC. This two dimensional (2D) problem serves as a training ground for developing, testing, and tuning the computational methodology. Knowledge acquired during the study of this example will then be applied in Sec. III B to scattering problems with much higher dimensionality.

A. One vibrational mode ($M=1$)

For $M=1$, stable propagation for times sufficient for bifurcation of the trajectory ensemble is obtained when the total number of trajectories exceeds 200. However, we used $N=500$ in these calculations in order to enhance the quality of the plots. An issue is how many trajectories are required in the stencil used for least squares fitting. Expansion of the stencil makes the propagation more stable but this requires additional computation time to compute the least squares expansion coefficients. As a result, accuracy and computational time must be compromised, especially for high dimensional problems. Through a number of trials, it was found that the minimum stencil size needed for stable propagation is related to the total number of trajectories through the relation $n_p=N/4$. Similarly, comparing the quantum trajectory results with those derived via direct integration of the time-dependent Schroödinger equation, the best values for the parameter ω in the weight function in Eq. (2.24) were found to lie in the range $\omega \approx 0.50-0.75$ a.u.

The initial wave packet in Eq. (2.19) was centered at $s_0=-3$ a.u. with width parameters $\beta_s=6.0$ a.u. and $\beta_{\rho 1}=6.75$ a.u. Then, as described above, this packet was discretized into an ensemble of quantum particles by random generation of coordinates according to the normal distribution (with the standard deviation $\sigma=0.35$). The translational energy was set to $E=3000\ \mathrm{cm}^{-1}$ and the ensemble was launched toward the barrier. The system of Eqs. (2.16) and (2.17) (with the reduced mass $\mu=2000$ a.u. and force constant $k_{01}=0.0911$ a.u.) were integrated with the first-order Euler explicit time propagator (the time step $\Delta t=4$ a.u. was used). The curvature parameters in Eq. (2.1) were set to the values $R(0)=4.5$ and $\alpha=0.01$.

When the ensemble reaches the curved region of the reaction path near $s=0$, it starts asymmetric bouncing from the walls of the vibrational valley. The ensemble develops a "snaking" motion, shown in Fig. 2, which Marcus referred to as the bobsled effect [17]. The leading edge of the ensemble enters into the region of high vibrational energy at

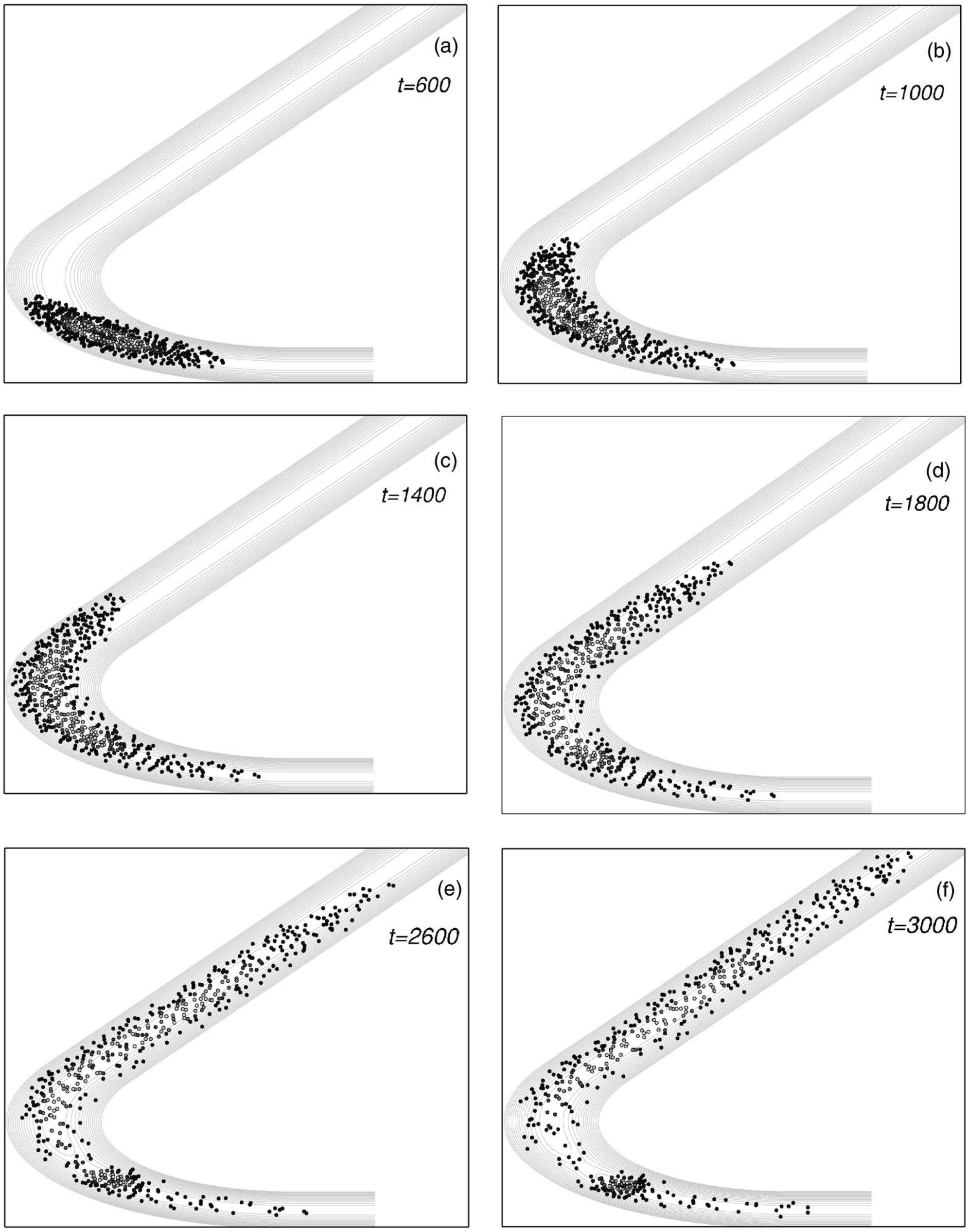

FIG. 2. Snapshots of quantum trajectories in Cartesian coordinates for one vibrational mode (barrier height $V_0 = 1000\ \mathrm{cm}^{-1}$) at six time steps (in a.u.): (a) $t = 600$, (b) $t = 1000$, (c) $t = 1400$, (d) $t = 1800$, (e) $t = 2600$, and (f) $t = 3000$. Contours of the potential energy are also shown.

$t = 600$ a.u. while the remainder of the ensemble is concentrated around the minimum of the potential. Then, the center of the ensemble follows along the path formed by the leading edge. The latter is pushed back toward lower energies at $t = 1000$ a.u. This process is repeated and again at $t = 1400$ a.u. the leading edge penetrates into the high vibrational energy region after "rolling down" the product side of the potential energy barrier. Snaking continues at later times as the transmitted packet moves further into the product valley. Snaking may cause some problems for trajectory propagation when the curvature is large since the edge particles are sensitive to sudden changes in motion and this may cause them to deviate significantly from the RC. Of course, distant particles located far from the RC carry a very low density and decrease the stability of the propagation. Therefore, these outlying trajectories were eliminated from the ensemble. The criterion is that if $|\rho_1| > 1.2$ a.u., this trajectory is removed from the ensemble.

Figure 3 shows a comparison between the quantum trajectory results and the "exact" probability density obtained by direct integration of the time-dependent Schroödinger equation on a large space fixed grid. For plotting purposes, the RC has been "stretched out," so that s and ρ_1 appear as rectilinear coordinates. As can be seen, at $t = 1400$ a.u., before nodes form in the reflected region, the entire ensemble of quantum particles is in good agreement with the exact result. At a later time, $t = 2400$ a.u., the transmitted part remains accurate while the reflected packet has lost accuracy

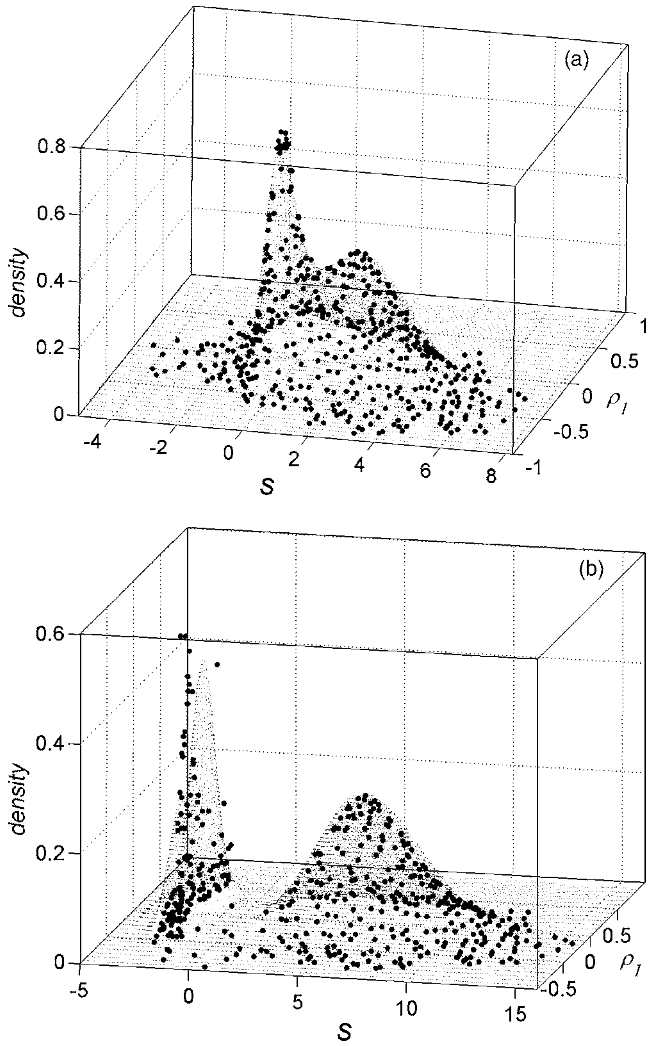

FIG. 3. Probability densities derived from grid integration of the time-dependent Schroödinger equation (surface map) and quantum trajectories (points) (barrier height $V_0 = 2000\ \mathrm{cm}^{-1}$) at two time steps: (a) $t = 1400$ and (b) $t = 2400$. The coordinates and time are given in a.u.

due to multiple node formation. In spite of this, the transmission probabilities can be computed accurately. Using the Monte Carlo technique described in Sec. II F, the probability density was integrated over the region occupied by the transmitted subensemble to yield transmission probabilities. These time-dependent probabilities, shown in Fig. 4 for three barrier heights, are in good agreement with the exact results. This example is a good test for Monte Carlo integration since its results can be compared with those derived by accurate integration methods which are appropriate for regular grids.

B. Multiple vibrational modes ($M = 5$ and 25)

The algorithm used to study reactive scattering for a system with one vibrational mode can be readily extended to a much larger number of modes. When setting up initial conditions on the trajectories, it is not necessary to cover each coordinate direction with a large number of grid points. In this unfavorable case, the total number of points would scale roughly as $\langle N\rangle^{M+1}$, where $\langle N\rangle$ is average number of points along each coordinate. However for an irregular mesh, the scaling of computational effort is defined solely by the basis set, which is chosen to scale linearly with the number of modes. This feature is a significant advantage of using an irregular mesh in the study of multidimensional problems. In order to estimate the minimal number of trajectories needed for stable propagation for this particular model, the stencil size n_p needs to be multiplied by 4 since $n_p = N/4$, as mentioned previously. In addition, we have the least squares requirement, $n_p > n_b$, and normally n_p should exceed n_b by about a factor of three in order to stabilize the propagation. Taking into account that $n_b = 2M + 7$, the required number of trajectories for M vibrational modes is estimated to be $N \approx 12(2M + 7)$. For example, the highest number of vibrational modes for which stable propagation can be run with 500 particles is 17.

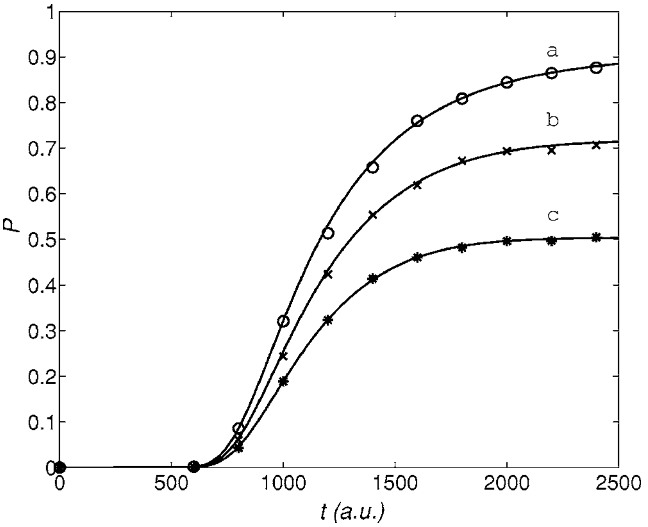

FIG. 4. Comparison of time-dependent reaction probabilities from direct integration of the Schrodinger equation (curves) with those from quantum trajectory calculations (points) for $M = 1$ at three barrier heights (in cm^{-1}): (a) $V_0 = 1000$, (b) $V_0 = 2000$, and (c) $V_0 = 3000$.

Computations were performed for $M = 5$ with $N = 500$ and $M = 25$ with $N = 1000$. If the parameters are set to the optimal values as described above for the $M = 1$ case, then the time propagation is stable. The computational results demonstrate many features in common with the $M = 1$ case. Projection of the trajectories into the (s, ρ_1) plane again reveals snaking since this vibrational motion is coupled with translational motion by curvature terms. However, projections onto other subspaces where the coordinates are coupled only via translation-vibration terms in the potential energy shows that the trajectories oscillate symmetrically along the vibrational coordinates.

After a sufficient period of time, the trajectory ensemble bifurcates along the translational coordinate. Projection of the trajectories into the three-dimensional (s, ρ_1, ρ_2) subspace is shown in Fig. 5 for $M = 5$ and $V_0 = 2000\ \mathrm{cm}^{-1}$. The size of each ball in this figure is proportional to the value of the C amplitude. Since this ensemble is a projection from six di-

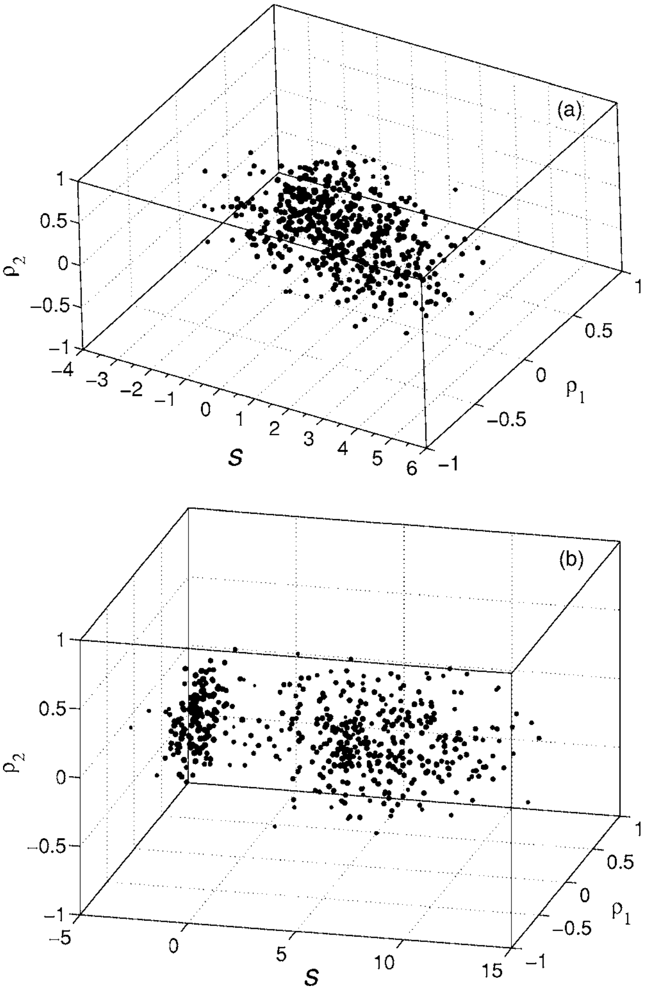

FIG. 5. Projection of quantum trajectories into the three dimensional (s,ρ_1,ρ_2) subspace for $M=5$ at two time steps: (a) $t=1200$ and (b) $t=2400$. The barrier height is $V_0=2000$ cm^{-1}. The coordinates and time are given in a.u.

mensional (6D) onto a three dimensional (3D) subspace, some edge trajectories carry large density while some interior ones have a small density. Careful examination of Fig. 5(a) reveals that snaking can be seen at $t=1200$ a.u. The leading edge is stretched toward the region of negative values of ρ_1. The mean value of ρ_1 (for the entire ensemble) at this time is $\langle\rho_1\rangle=-0.1$ a.u. At the later time shown in Fig. 5(b) ($t=2400$ a.u.), complete bifurcation is observed along the translational coordinate. Most of the reflected trajectories carry large density values. The transmitted part is smooth and the trajectories are distributed close to the normal distribution along each coordinate. The mean values for the coordinates for the transmitted sub-ensemble are: $\langle s\rangle=5.82$ a.u., $\langle\rho_1\rangle=-0.14$ a.u., $\langle\rho_j\rangle\approx 0$ a.u. for $j=2-5$. This set of mean values was used for the p density in Monte Carlo integration.

This calculation required 7.4 min of CPU time on a 2.4 GHz Pentium-4 to propagate the ensemble. The least squares routine itself takes 82% of this time and stencil sorting requires 12%. Notice that the latter routine was called only 30 times since new stencil organization occurs at intervals of 20 time steps. Matrix inversion of P^twP [see Eq. (2.23)] is not the slowest step for this computation since its size is only 17×17. The slowest process is P-matrix organization (size 125×17) with its following multiplication by the diagonal weight-matrix w (size 125×125) and the transpose P^t (size 17×125). The total computational time grows almost linearly with the number of vibrational modes if the total number of trajectories is fixed.

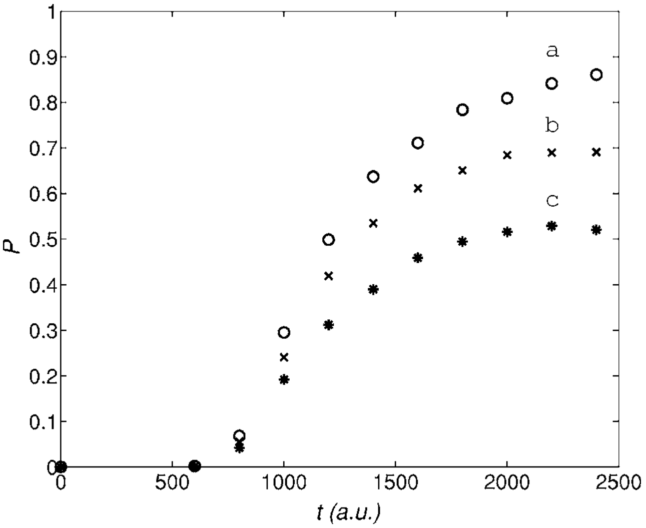

FIG. 6. Time-dependent reaction probabilities for $M=25$ at three barrier heights (in cm^{-1}): (a) $V_0=1000$, (b) $V_0=2000$, and (c) $V_0=3000$.

Monte Carlo integration takes 3% and 24% of the total computational time if the number of Monte Carlo points is $N_{mc}=10^4$ and $N_{mc}=10^5$, respectively. However, for lower values of M, the relative time of Monte Carlo integration grows because propagation requires less of the computational time. For example, for $M=5$ the percentage of Monte Carlo integration is 10% and 51% when $N_{mc}=10^4$ and $N_{mc}=10^5$, respectively.

The time-dependent reaction probabilities for $M=25$ are shown in Fig. 6 for three barrier heights (in cm^{-1}): $V_0=1000$, 2000, and 3000. For the two larger barriers, these probabilities grow smoothly with time and then reach constant values after $t=2000$ a.u. For the lowest barrier case, the probability is still growing at this time because the packet has not completely bifurcated. Further propagation brings the transmission probability to a constant value as well. As can be seen, the points in this plot do not precisely lie along imaginary interpolated curves. As for one vibrational mode, these small deviations are the result of node formation in the reflected region. The nodal region in the reflected packet may affect the transmitted part (especially at high barrier heights) via trajectories that lie on the "back edge" of the transmitted packet. The interpolated density around the barrier region has some "kinks" and as a result, Monte Carlo integration gives slightly overestimated values of the transmission probabilities. Upon removal of a small number of these kinky edge particles from the transmitted packet, the transmission probabilities become constant after bifurcation, as they are supposed to be.

IV. SUMMARY

In this study, it was demonstrated that the quantum reaction dynamics of multidimensional quantum systems can be successfully described by propagating ensembles of quantum trajectories. The computational methodology was developed and applied to model reactive scattering systems in which the total dimensionality ranged from 2 to 26. The computational time scaled almost linearly with the number of vibrational modes. The longest computation, for $M=25$ with $N=1000$ trajectories, $n_b=250$ stencil size, and 600 time steps, required 118 min of CPU (on the same computer mentioned earlier). The most time consuming routine involved derivative evaluation by the least squares method. This procedure involves matrix inversion and (for large M) the computational effort scales as $(2M+7)^3$. As a result, its percentage of the total computational time is expected to grow significantly for higher dimensionality. One way to reduce the computational effort is to use least squares fitting coefficients derived for a fiducial trajectory for a set of nearby trajectories within the same stencil. This approximation has been tested and appears to be useful for studying systems with more than 25 vibrational modes.

Although in the current study we dealt with reactive scattering problems involving up to 26 degrees of freedom, this value is not an upper limit for the algorithm. In principle, the procedures described here can be applied to systems with much higher dimensionalities. Results for larger model reactive systems, those with several hundred degrees of freedom, will be reported in future publications [23]. Quantum trajectory studies using accurate potential energy surfaces are feasible, as demonstrated recently for $O(^3P)+H_2$ reactive scattering [15].

ACKNOWLEDGMENT

The Robert Welch Foundation is thanked for generously supporting this research.

---

[1] R. E. Wyatt, J. Chem. Phys. **111**, 4406 (1999).

[2] D. Nerukh and J. H. Frederick, Chem. Phys. Lett. **332**, 145 (2000).

[3] B. K. Dey, A. Askar, and H. A. Rabitz, J. Chem. Phys. **109**, 8770 (1998).

[4] F. Sales Mayor, A. Askar, and H. A. Rabitz, J. Chem. Phys. **111**, 2423 (1999).

[5] R. E. Wyatt, *Quantum Dynamics with Trajectories: Introduction to Quantum Hydrodynamics* (Springer, New York, 2005), pp. 211–215.

[6] R. E. Wyatt and K. Na, Phys. Rev. E **65**, 016702 (2002).

[7] B. K. Kendrick, J. Chem. Phys. **121**, 2471 (2004).

[8] D. K. Pauler and B. K. Kendrick, J. Chem. Phys. **120**, 603 (2004).

[9] D. Babyuk and R. E. Wyatt, Chem. Phys. Lett. **400**, 145 (2004).

[10] D. Babyuk and R. E. Wyatt, J. Chem. Phys. **121**, 9230 (2004).

[11] J. B. Maddox and E. R. Bittner, J. Chem. Phys. **119**, 6465 (2003).

[12] S. Garashchuk and V. Rassolov, Chem. Phys. Lett. **376**, 358 (2003).

[13] S. Garashchuk and V. Rassolov, J. Chem. Phys. **120**, 1181 (2004).

[14] S. Garashchuk and V. Rassolov, J. Chem. Phys. **120**, 6815 (2004).

[15] V. Rassolov, S. Garashchuk, and G. Schatz, J. Phys. Chem. A (to be published).

[16] R. E. Wyatt, Ref. [5], pp. 127–132.

[17] R. A. Marcus, J. Chem. Phys. **45**, 4493 (1966); **45**, 4500 (1966).

[18] W. H. Miller, N. C. Handy, and J. E. Adams, J. Chem. Phys. **72**, 99 (1980).

[19] G. M. Strang, *Introduction to Applied Mathematics* (Wellesley-Cambridge Press, Wellesley, MA, 1986), pp. 78–79, 103–106, 382–397.

[20] G. H. Golub and C. F. Van Loan, *Matrix Computations* (Johns Hopkins University Press, Baltimore, 1996), pp. 69–74, 206–269.

[21] W. H. Press, B. P. Flannery, S. A. Teukolsky, and W. T. Vetterling, *Numerical Recipes in Fortran* (Cambridge University Press, Cambridge, 1992), pp. 34–40.

[22] W. H. Press, Ref. [21] pp. 306–307.

[23] D. Babyuk and R. E. Wyatt, J. Chem. Phys. (to be published).